A Control Framework for Accurate Mechanical Impedance Rendering with Series-Elastic Joints in Prosthetic Actuation Applications

Isaac Harris¹, Elliott Rouse^{1,2}, Robert D. Gregg², and Gray Cortright Thomas^{2,3,*}

Abstract—In addition to lifting up the body during gait, human legs provide stabilizing torques that can be modeled as a spring-damper mechanical impedance. While powered prosthetic leg actuators can also imitate spring-damper behaviors, the rendered impedance can be quite different from the desired impedance, stemming from unmodeled transmission characteristics (e.g., sliding friction, bearing damping, gear inefficiency, etc.). Moreover, for powered prostheses to mimic human joint impedance, they will need actuators that accurately render a wide range of mechanical impedances in a variety of ground contact conditions, including nearly free-swinging behavior in swing phase and stiff spring-like behavior in stance phase. For series-elastic prosthetic leg actuators, as in Open-Source Leg (OSL), these sudden output inertia changes present a challenge for traditional cascaded impedance control. In this paper we propose a solution based on disturbance observers (DOBs) and full-state feedback (FSF) impedance control. The DOB serves to mask transmission imperfections, while the FSF controller (via pole-zero placement) specifies the actuator impedance that couples to the uncertain joint inertia. We validate our control framework on an OSL-like two-actuator dynamometry testbed.

Index Terms—Compliance and impedance control, compliant joints and mechanisms, prosthetics

I. INTRODUCTION

OSS of a lower limb is a growing problem that prevents millions of Americans from performing activities of daily life [1]. Fortunately, powered prosthetic devices have shown promise in recovering lost functionality [2] and are consistently improving in both mechanical design and control. However, there are still many limitations which can lead to disuse of devices, fear of falling [3] and avoidance of activities [4]. Bio-mimetic feedback control—or the ability to accurately reproduce the natural dynamics and reflexes of biological limbs—remains amongst these limitations despite the wide range of control paradigms applied to prostheses [5]. And this suggests a gap in the control strategies available for the actuation sub-components of modern prosthetic legs.

Impedance control [6], or the achievement of virtual springdamper behaviors in robot manipulators, is a natural choice

Manuscript received: January 15, 2024; Revised: April 25, 2024; Accepted: May 24, 2024.

This paper was recommended for publication by Editor Pietro Valdastri upon evaluation of the Associate Editor and Reviewers' comments. This work was supported by NSF award numbers 2024237, 1953908, and 1830338.

¹Department of Mechanical Engineering, University of Michigan, Ann Arbor, MI 48109, USA. ²Department of Robotics, University of Michigan, Ann Arbor, MI 48109, USA. ³Department of Mechanical Engineering, Texas A&M University, College Station, TX 77840, USA. *gthomas@tamu.edu

Digital Object Identifier (DOI): see top of this page.

for solving this problem. A typical "impedance-controlled" prosthetic leg will use a finite state machine (FSM) to switch between different mechanical impedance values such as a bent knee target for swing and a straight knee target for stance [5], [7]. More recently, prosthesis controllers have begun to employ continuously varying impedance control parameters [8]–[12]. (And this potentially allows replication of the time-dependent perturbation responses that have been measured during walking [13]–[16] instead of the quasi-stiffness that best smooths out the discrete phases of an FSM [17].) Ultimately, both approaches rely on the accurate rendering of mechanical impedance behaviors using actuator-level control.

Traditionally, actuators for prostheses have used a small high-speed motor with a highly geared transmission as in [7]. This allows for lightweight designs, but the transmission dynamics can result in inaccurate impedance rendering. Quasi-Direct Drive (QDD) motors, for example as used in [18], rely on larger, heavier motors with a lower ratio transmission to more directly achieve the required joint torque. This greatly improves impedance rendering quality, but comes at the cost of increased weight and size. To improve the quality of impedance rendering in either QDD or traditional systems, unmodeled actuator characteristics, such as sliding friction, bearing damping, or gear inefficiency, need to be compensated for. Unaddressed, these issues can significantly degrade control accuracy even for relatively low gear ratios, as exemplified by the open loop impedance control results in [19].

Feedback control of measured actuator torque is a key strategy for overcoming actuator model uncertainty. And Series-Elastic Actuators (SEAs) are a common sensing approach that also provides additional benefits like energy recovery [20]–[23]. Utilizing a reduction ratio of 50:1, the Open Source Leg (OSL) [2] includes an SEA for exactly these reasons, making it an ideal candidate for researching impedance control paradigms in the wearable robotics space. However, the addition of the spring module complicates the impedance control of the device.

Typically, SEA controller design uses a cascade of torque and position feedback [24]–[26]. This framework is effective for applications requiring only one type of impedance behavior. However, the cascaded control assumption—that the inner loop has higher bandwidth than the outer loop—restricts the capabilities of these controllers [27]. If the faster inner loop is a position controller, stiffer impedances are more accurately rendered. And conversely, if the inner loop is a torque controller, soft impedances are more accurately

rendered. Additionally, variability in output inertia will change the closed-loop dynamics of the inner loop, further reducing the practicality of the cascade. These trade-offs are problematic for humanoids and other robots which have reason to switch between extreme impedance behaviors and experience changing inertia due to intermittent ground contact [28], [29].

Non-cascaded, full-state feedback (FSF) controllers avoid these structural limitations, and are capable of generalizing cascaded controllers at the cost of some additional complexity in their tuning [30]–[32]. However, when FSF control is used instead of cascaded control, some pole and zero placements will result in gain settings that do not sufficiently attenuate unmodeled transmission dynamics. This ultimately results in poor impedance rendering performance and is most apparent with gain settings that resemble neither of the two common cascade approaches.

To deal with unmodeled dynamics, e.g., "internal" disturbances like friction, recent SEA controllers have been equipped with disturbance compensating filters known as disturbance observers (DOBs). DOBs work by indirectly measuring the disturbances to a nominal plant G(s) and compensating for them. The measurement is achieved by comparing lowpass filtered plant input to low-pass filtered plant output that has gone through a plant-inverse filter (the combination of the low pass filter Q(s) and the plant-inverse filter allows the combined system $Q(s)G^{-1}(s)$ to be a causal system). The framework then feeds the estimate of input disturbance back into the input of the plant, attenuating the magnitude of the disturbance completely at frequencies where $Q(s) \approx 1$. DOB techniques have been central to state-of-the-art cascaded controllers [33]–[36]. But such approaches remain limited by the cascade structure when faced with a range of impedance targets and output inertias. The DOB technique has also been applied in FSF controllers for position control [37] and human strength amplification [38]. However, FSF controllers with a DOB have yet to be validated in rendering a target perturbation response.

In this paper, we introduce a DOB and FSF framework for accurate impedance rendering in prosthetic joints with SEAs. Adopted from the two-pole two-zero placement strategy for designing full-state SEA feedback controllers [39], this framework adds a DOB for the motor and transmission subsystem. The addition of the DOB primarily serves to reduce various unmodeled friction effects with the added benefit of compensating for other plant model uncertainties (e.g. imperfect estimates of motor resistance or torque constant). Additionally, we re-frame as a voltage control problem which provides "free" electrical damping from the motor back emf, and synthesize our DOB in discrete time to more accurately capture the time delay inherent to our digital controller. We validate this approach in the context of prosthesis control using SEA testbed hardware which simulates the transmission and spring-fixture of the Open-Source Leg (OSL) [2]. Results demonstrate 1) online attenuation of transmission friction and 2) the successful superposition of a mechanical impedance on top of biomechanical position and torque trajectory tracking.

TABLE I Symbol Glossary

Symbol	Meaning		
ϕ_a	knee motor position		
ϕ_{j}	environment motor position		
\hat{N}	transmission ratio		
θ_a, θ_j	motor output angles (reflected by N)		
J, b	inertia and damping, motor-frame		
$ au_s$	spring torque		
V_a, I_a	motor voltage and current		
R	motor electrical resistance		
K_t	motor torque constant		
K_s	spring stiffness		
K_1, B_1, K_2, B_2	controller parameters (constant)		
$\tilde{K}_1, \ \tilde{B}_1, \ \tilde{K}_2, \ \tilde{B}_2$	compliance shape parameters (constant)		
T_s	time step		

II. MODELING AND CONTROL

A. System Model

The testbed simulates two systems: the OSL knee SEA and the rest of the environment in which it is designed to operate (see Fig. 1), *i.e.*, the residual limb of a person with transfemoral amputation moving through a periodic walking behavior with intermittent ground contact.

We model the continuous dynamics of the SEA as

$$J\ddot{\phi_a} = K_t I_a - b\dot{\phi_a} + N^{-1}\tau_s,\tag{1}$$

$$V_a = RI_a + K_t \dot{\phi}_a, \tag{2}$$

$$\tau_s = K_s(\theta_i - \theta_a),\tag{3}$$

$$\phi_a = N\theta_a, \ \phi_j = N\theta_j, \tag{4}$$

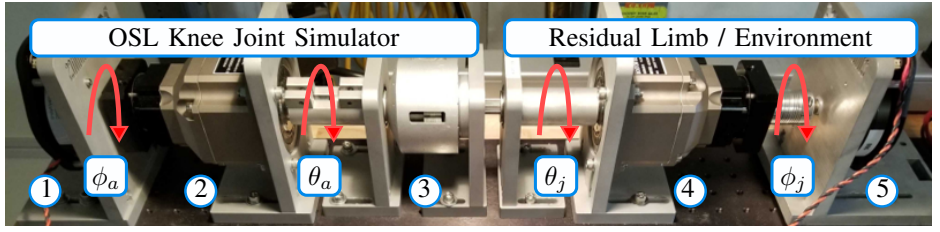
with variables as defined in Tab. I. Essentially, ideal DC motors, (1) and (2), are coupled by a spring (3) in between corresponding transmissions (4). The DC approximation of the brushless DC motors is made possible by the q-axis DC representation [40], [41]. Combining (1-4) and applying the Laplace Transform, the actuator plant with input V_a and output ϕ_a (and for input V_j to output ϕ_j) is

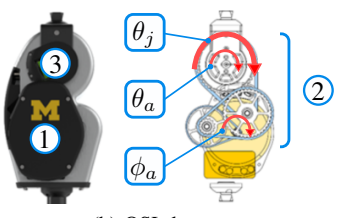
$$G(s) = \frac{K_t R^{-1}}{Js^2 + (b + K_t^2 R^{-1})s + K_s N^{-2}},$$
 (5)

and the corresponding representation of the spring-rate as transforming opposite-side motor-angle to a voltage (see Fig. 2) is

$$\Psi = \frac{RK_s}{K_t N^2}.$$
(6)

Together, (5-6) provide an actuator model with two inputs: commanded motor voltage, V_a , and the opposing motor position, ϕ_j or the opposite combination (V_j and ϕ_a). The interconnections of these transfer functions is shown in Fig. 2. Note that (6) converts ϕ_j to an effective voltage felt by the motor (*i.e.*, the change in motor voltage that would produce the same change in motor acceleration as this change in spring output position).





(a) SEA Testbed Apparatus

(b) OSL knee

Fig. 1. SEA Testbed Apparatus (a) emulates both a prosthetic knee joint and its environment. The joint simulator is designed to mimic the OSL knee (b), consisting of an identical motor (1), a planetary gear transmission with matching transmission ratio (2), and an identical series spring assembly (3). The SEA is coupled to another planetary gear transmission (4) and electric motor (5) which simulate the environment and all external forces on the joint of the prosthetic leg. In this antagonistic configuration, it is possible to measure the response of the prosthetic leg joint to environmental perturbations and evaluate controllers that are expected to imitate human-like mechanical impedance in response to such perturbations.

B. Controller

The impedance controller consists of three parts: (1) a feed-forward trajectory generator, (2) a DOB for attenuating unmodeled dynamics, and (3) an FSF controller used to achieve biomimetic impedance.

1) Nominal Trajectory Generation: The goal of the nominal trajectory generator is to produce the a-priori voltage signal time series for the two motors, $u_k \in \mathbf{R}^2$, that will achieve desired joint angle and joint torque trajectories, y_k , in the absence of disturbances and nonlinearities. This becomes a non-trivial model inversion problem which can be achieved by analyzing the coupled dynamics of both motors in state space representation given by the LTI system

$$\dot{x} = Ax + Bu,
 y = Cx.$$
(7)

where

$$A = \begin{bmatrix} 0 & 1 & 0 & 0 \\ -\alpha & \beta & \alpha & 0 \\ 0 & 0 & 0 & 1 \\ \alpha & 0 & -\alpha & \beta \end{bmatrix}, \quad x = \begin{bmatrix} \phi_a \\ \dot{\phi}_a \\ \phi_j \\ \dot{\phi}_j \end{bmatrix},$$

$$B = \frac{K_t}{JR} \begin{bmatrix} 0 & 0 \\ 1 & 0 \\ 0 & 0 \\ 0 & 1 \end{bmatrix}, \quad u = \begin{bmatrix} V_a \\ V_j \end{bmatrix},$$

$$C = \frac{1}{N} \begin{bmatrix} -K_s & 0 & K_s & 0 \\ 0 & -K_s & 0 & K_s \\ 0 & 0 & 1 & 0 \\ 0 & 0 & 0 & 1 \end{bmatrix}, \quad y = \begin{bmatrix} \tau_s \\ \dot{\tau}_s \\ \theta_j \\ \dot{\theta}_j \end{bmatrix},$$

and

$$\alpha = K_s/JN^2, \quad \beta = -J^{-1}(b + K_t^2/R).$$
 (8)

To account for the delay between consecutive motor voltage commands, we convert (7) to a discrete time representation with a ZOH on the input and sample time, T_s (i.e., voltage commands are assumed constant between time steps). The discretized model is given by

$$x_{k+1} = A_k x_k + B_k u_k, (9)$$

$$y_k = Cx_k, (10)$$

where the discrete-time matrices can be calculated according to a zero-order hold assumption on the input as

$$A_k = e^{AT_s}, (11)$$

$$B_k = \int_0^{T_s} e^{A\tau} B d\tau. \tag{12}$$

Next, to find the voltage signals which correspond to nominal joint angle and joint torque trajectories, we must invert (9). There are multiple strategies which yield satisfactory y_k , but given the digital nature of our controller, we utilized the discrete-time controllability matrix, M_n , where

$$M_n = \begin{bmatrix} B_k, & A_k B_k, & \cdots, & A_k^{n-1} B_k \end{bmatrix}, \tag{13}$$

for an n-step ahead state prediction. If M_n has full row rank $(i.e., \operatorname{rank}(M_n) = \dim(x_k) = 4)$, then x_{k+n} can be arbitrarily placed. Ideally, we would like full control over x_{k+1} , but the corresponding controllability matrix, $M_1 = B_k$, only has rank 2. To achieve full row rank, we loosen our constraint to full controllability of x_{k+2} which is given by

$$x_{k+2} = A_k^2 x_k + B_k u_{k+1} + A_k B_k u_k, \tag{14}$$

$$M_2 = \begin{bmatrix} B_k, & A_k B_k \end{bmatrix}. \tag{15}$$

Since M_2 is full row rank, it permits model inversion. Taking advantage of the fact that C is square and invertible, we rewrite (14) using (10) and (15) to obtain the input vector $\hat{u} \in \mathbb{R}^4$ where

$$\hat{u} = \begin{bmatrix} u_{k+1} \\ u \end{bmatrix} = M_2^{-1} (C^{-1} y_{k+2} - A_k^2 C^{-1} y_k), \tag{16}$$

i.e., the exact solution for the discrete feed-forward input that brings the system output from y_k to y_{k+2} . While this inversion method technically only provides half the desired resolution in our output signal, for small sample times and continuous target behaviors, y[m] approaches the desired signal, y[n].

It should be noted that an asymmetric pair of actuators could have been used on the testbed without significantly altering the model. For the primary function of performing impedance tests, a mirrored setup was sufficient as we only needed to apply small perturbations on top of the knee motors trajectories. However, if a broader range of perturbations were desired, a second pair of equations, identical in structure to (5) and (6), would represent the environment actuator and state space equations (7) and (8) would contain two sets of actuator constants instead of one.

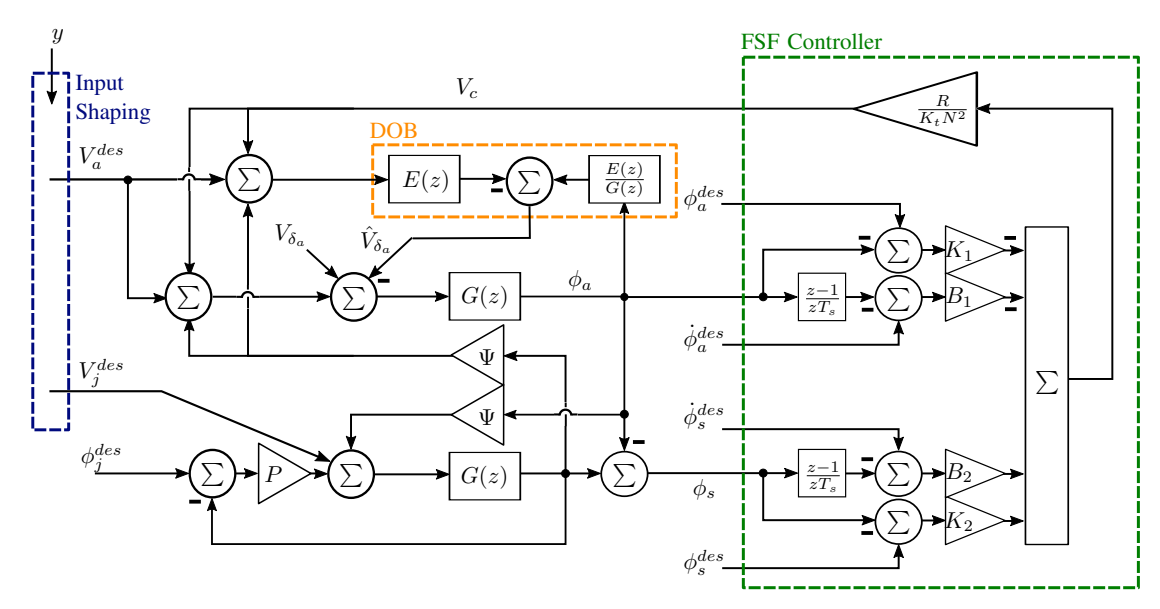


Fig. 2. Controller block diagram—the prosthetic joint's actuator plant, G(z), is surrounded by a disturbance observer (DOB) which attenuates a frictional disturbance, $V_{\delta a}$. The system input, y, contains a-priori joint trajectories and desired feed-forward voltages, V_a^{des} and V_j^{des} . A full-state feedback controller (FSF Controller) is used to shape the mechanical impedance of the prosthetic joint. Note that, while the simple discrete derivative operator, $(1-z^{-1})/T_s$, is used in the block diagram, differentiation is actually accomplished by the Dephy ActPack motor driver at a higher sampling rate than the main controller.

2) Disturbance Observer: A DOB wraps the nominal actuator model given by (5), allowing the feed-forward trajectory generator and FSF controller to assume a pristine model without friction and other imperfections [42]. The largest unmodeled disturbance present in our testbench is static friction from the gear boxes. Additionally, there is plant uncertainty in the estimates of K_t , b, J, R, etc.

Using (5) and (6), a typical continuous-time DOB can be constructed for the actuator model which has the form

$$\hat{V}_{\delta_a} = \frac{Q(s)}{G(s)}\phi_a - Q(s)(V_a^{des} + \Psi\phi_j - \hat{V}_{\delta_a}), \quad (17)$$

where Q(s) is a second order low pass filter with cutoff frequency, ω , and damping ratio, ζ ,

$$Q(s) = \frac{w^2}{s^2 + 2\zeta\omega + \omega^2}. (18)$$

This low pass filter serves the dual purpose of reducing high frequency measurement noise and preserving causality despite inverting G. The DOB's output, \hat{V}_{δ_a} , can be subtracted from the voltage effort issued by the feed-forward and FSF controllers, V_a^{des} , to attenuate any effects that unmodeled friction or parameter uncertainty would otherwise have on the output.

To adapt this continuous-time DOB to our digital control system, we solve (17) for

$$\hat{V}_{\delta_a} = \frac{E(s)}{G(s)}\Theta_a - E(s)(V_a^{des} + \Psi\Theta_p), \tag{19}$$

$$E(s) = \frac{1}{Q^{-1} - 1}. (20)$$

Next, we obtain the discrete transfer function, E(z), by a three step process: 1) convert E(s) to state space controllable canonical form, 2) use (11) and (12) to obtain discrete matrices, and

3) convert back to transfer function representation. The same process is applied to G(s) to obtain G(z), which then allows us to write the full expression for the discrete DOB output as

$$\hat{V}_{\delta_a} = \frac{E(z)}{G(z)} \phi_a - E(z) (V_a^{des} + \Psi \phi_p), \tag{21}$$

which is shown in context in Fig. 2.

C. Full-State Feedback Compliance Shaping

1) Control Structure: To accurately render biomimetic impedance, we adopt the compliance shaping paradigm developed in [39]. This method involves manipulating the gains of an FSF control law with the following structure:

$$V_c = \frac{R}{K_t N^2} \Big((K_2 + B_2 s) \Delta \phi_s - (K_1 + B_1 s) \Delta \phi_a \Big), \quad (22)$$

$$\Delta \phi_s = \Delta \phi_j - \Delta \phi_a, \quad \Delta \phi = \phi^{des} - \phi.$$
 (23)

By feeding back the entire state, we can arbitrarily place the poles and zeros of the actuator's integral admittance transfer function, $\theta_j/\tau_s(s)$ —the more convenient, causal representation of its mechanical impedance. This transfer function is

$$\frac{\theta_j}{\tau_s} = \frac{\hat{J}s^2 + (\hat{b} + B_1 + B_2)s + (K_s + K_1 + K_2)}{(\hat{J}s^2 + (\hat{b} + B_1)s + K_1)K_s}, \quad (24)$$

where

$$\hat{J} = JN^2, \quad \hat{b} = bN^2 + K_t^2 N^2 R^{-1}.$$
 (25)

To construct (24), one can use (1-4) where (2) is equal to the new FSF control law given by (22).

Changing variables as in [38], we obtain its monic form (which lends itself to frequency domain tuning),

$$\frac{\theta_j}{\tau_s} = \frac{s^2 + \tilde{B}_2 s + \tilde{K}_2}{(s^2 + \tilde{B}_1 s + \tilde{K}_1) K_s},\tag{26}$$

5

where

$$K_{1} = \hat{J}\tilde{K}_{1}, \quad K_{2} = \hat{J}\tilde{K}_{2} - \tilde{K}_{1} - K_{s},$$

$$B_{1} = \hat{J}\tilde{B}_{1} - \hat{b}, \quad B_{2} = \hat{J}\tilde{B}_{2} - B_{1} - \hat{b}.$$
 (27)

Ultimately, this controller is used to shape the closed loop joint compliance

$$\frac{\theta_j}{\tau_j} = \frac{s^2 + \tilde{B}_2 s + \tilde{K}_2}{J_j s^2 (s^2 + \tilde{B}_2 s + \tilde{K}_2) + K_s (s^2 + \tilde{B}_1 s + \tilde{K}_1)}, \quad (28)$$

so that it emulates the compliance of a biological knee joint

$$C_k(s) = \frac{1}{J_k s^2 + B_k s + K_k}. (29)$$

2) Frequency Domain Shaping: The controller gains present in (26) are tuned by analyzing its transfer function in the frequency domain. The design space is constrained by four factors: 1) the target knee stiffness, K_k , which necessitates a low frequency asymptote equal to K_k^{-1} , 2) the target knee damping, B_k , which governs the placement of a low frequency pole, 3) the stiffness of the physical series-elastic element, K_s , which necessitates a high frequency asymptote equal to K_s^{-1} , and 4) the practical limitation of the controller's update rate, f_u , equal to 450 Hz and the related Nyquist frequency of $f_u/2$. Since most of the poles and zeros in the resulting system are achieved via delayed feedback, we intentionally limit these pole and zero placements to be 50 Hz or less, well below the Nyquist frequency. Example values for K_k and B_k , equal to $50 \ Nm/rad$ and $1.59 \ Nm/rad/s$ respectively, are loosely within the realm of plausible human impedance values based on stiffness from [43] and damping ratio from [44].

We start by choosing our two poles, with the lower frequency pole, p_1 , given directly by the target biological impedance, and the high frequency pole, p_2 , at 50 Hz,

$$p_1 = \frac{K_k}{B_k}, \quad p_2 = \frac{\pi f_u}{4}.$$
 (30)

Given the asymptotic high and low frequency behaviors, these two poles define two lines that cross in the Bode plot. We connect these two lines with a pair of critically damped zeroes

$$\omega_z = \sqrt{\frac{1}{DB_k}}, \quad D = \frac{1}{K_s p_2}.$$
 (31)

Finally, we can extract the gains which comprise (26) using the following relationships

$$\tilde{K}_1 = p_1 p_2, \quad \tilde{B}_1 = p_1 + p_2,$$
 (32)

$$\tilde{K}_2 = \omega_z^2, \quad \tilde{B}_2 = 2\omega_z, \tag{33}$$

which can subsequently be used with (27) to obtain the final set of gains present in our FSF control law given by (22).

III. EXPERIMENTS

The SEA testbed (see Fig. 1) was used to conduct both frequency domain and time domain experiments. The testbed's knee simulator consists of three parts: 1) an OSL BLDC motor (ActPack, Dephy Inc. Boston, MA), 2) a 50:1 Gearbox (Boston Gear, Boston, MA) which matches the transmission ratio of the OSL knee, and 3) the OSL torsional spring carriage assembly

TABLE II EXPERIMENT PARAMETERS

Symbol	Value	Units		
J	2.0×10^{-4}	kgm^2		
b	1.16×10^{-3}	N m/rad/s		
K_t	0.14	Nm/A		
R	0.28	Ω		
N	50	-		
K_s	191	Nm/rad		
K_k	50.0	Nm/rad		
B_k	1.59	N m/rad/s		
K_1	4932.9	Nm/rad		
K_2	13719.7	Nm/rad		
B_1	-5.7	N m/rad/s		
B_2	21.4	N m/rad/s		

[2]. On the opposite side of the spring, another 50:1 Gearbox and OSL BLDC motor serve as the environment simulator.

Identical to the OSL's embedded system, a Raspberry Pi computer is responsible for logging data and orchestrating the high-level voltage commands sent to each motor's control board. During all experiments, ϕ_a and ϕ_j were measured using the embedded motor encoders with a resolution of $\pm 0.022^\circ$ and sampling rate of 450 Hz. From those two measurements, both τ_j and θ_j can be calculated using (3) and (4). Quantities for all experiment parameters can be found in Tab. II.

Both experiments utilize the environment actuator to perturb the knee actuator for the purpose of measuring impedance. We use "perturbation" to refer to external torques from the environment on the knee actuator while "disturbance" is reserved for "internal" disturbances compensated for by the DOB. For example, the external force of heel strike is a perturbation and the error in the motor torque constant, K_t , is a disturbance.

A. Frequency-Domain Validation

To measure the actual joint compliance rendered by our controller, wavelet perturbations in joint angle, θ_i , were applied to the knee actuator via the environment actuator. Each wavelet was generated with a single frequency component ranging from 0.5 to 50 Hz and an amplitude of 0.1 radians. DOB filter parameters f_q and ζ were set to 10Hz and 0.7, respectively. In between wavelets, a minimum pause of 2 seconds was included to allow the knee actuator to come to rest prior to the next perturbation. Following the experiment, a least squares method was used to convert τ_i and θ_i from time series data to their respective phasor representations in the complex plane. From here, phasors were divided to obtain point estimates of the transfer function. A confidence region was constructed by repeating the identification five times per frequency and displaying the one standard deviation spread in magnitude and phase. Performance was evaluated by the metric of root mean squared percent error (RMSPE) between the achieved and desired transfer functions. The error signal used when computing combined RMSPE was formed by first subtracting desired and measured impedance values in their complex form and then taking the magnitude. In contrast, the error signals used to compute magnitude RMSPE and phase RMSE were calculated with the magnitudes and phases of the complex numbers independently.

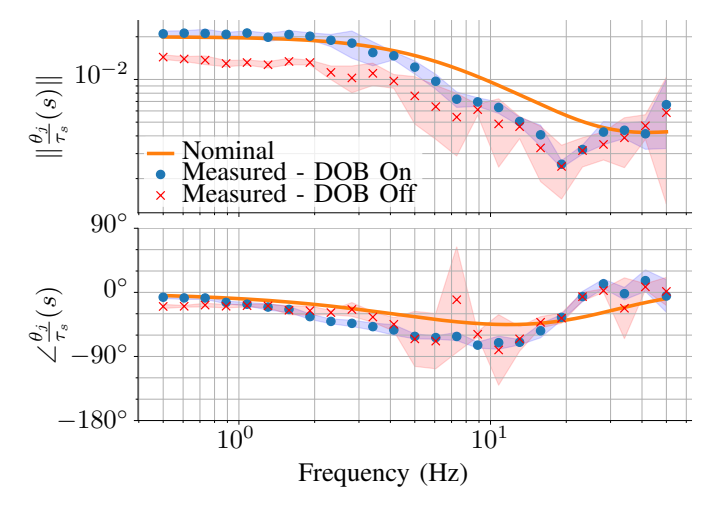


Fig. 3. Bode plots of the closed loop actuator—the 'DOB On' and 'DOB Off' empirical integral admittance transfer functions, $\theta_j/\tau_s(s)$, are measured using the wavelet identification experiment and compared to the desired (Nominal) behavior. At low frequency, $f_q=0.5$ Hz, the addition of the DOB significantly improved the controller's ability to render mechanical impedance, exhibiting a combined RMSPE of 8.9% in contrast to the DOB Off case which yielded a combined RMSPE of 36.3%. At higher frequencies, the DOB performance worsened but always maintained a lower combined RMSPE relative to the DOB Off case.

B. Time-Domain Demonstration

A time domain test was conducted to demonstrate the controller's capability to track biological knee signals and respond appropriately to perturbation. Joint angle and joint torque during level walking were used as the nominal trajectories. These signals were generated using data from [45], assuming a 1.2-second walking period¹ and 80kg body mass . Both an unperturbed and perturbed step were simulated for comparison. The perturbation was applied at the beginning of stance as a 3-second pulse in joint angle, with a 5-degree amplitude. DOB filter parameters f_q and ζ were set to 5 Hz and 1.5, respectively.

To analyze the accuracy of impedance rendering, we begin by defining another delta term

$$\Delta \theta_s = \theta_{s,p} - \theta_{s,u},\tag{34}$$

where the secondary subscripts, p and u, denote perturbed and unperturbed steps, respectively. Note, (34) compares measured values from two different steps, while (23) compares a measured value with a desired value for the same time sample. Next, we compute the difference in measured spring torque between the nominal and perturbed steps, $\Delta \tau_s$, which is given by,

$$\Delta \tau_s = K_s \Delta \theta_s, \tag{35}$$

and the difference in ideal knee torque, $\Delta \tau_k$ (i.e., the torque that would occur if the system exhibited the ideal knee impedance), which is given by

$$\Delta \tau_k = K_k \Delta \theta_s + B_k \Delta \dot{\theta}_s. \tag{36}$$

TABLE III
FREQUENCY DOMAIN TEST RESULTS, RMSE/RMSPE

f (Hz)	= 0.5		$\in [0.5, 5]$		$\in (0.5, 50]$	
DOB	On	Off	On	Off	On	Off
Mag.	7.2%	28.0%	11.8%	34.7%	31.1%	46.2%
Phase (Deg)	2.88°	15.6°	14.9°	12.2°	21.7°	30.1°
Combined	8.9%	36.3%	28.3%	38.7%	47.0%	53.2%

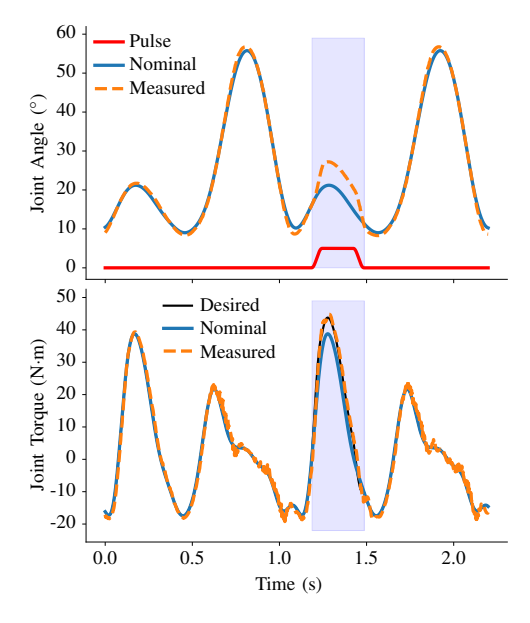


Fig. 4. **Time domain perturbation**—Top: the joint angle (θ_j) "Measured" follows the "Nominal" walking trajectory until perturbed by a "Pulse". Bottom: The actuator torque (τ_s) "Measured" follows the "Nominal" walking kinetics until perturbed. This "Measured" torque is similar (4.17 Nm RMSE) to the "Desired" torque due to the target perturbation response.

Thus we define our impedance accuracy using the error between those torque quantities as

$$\epsilon_{\tau} = \Delta \tau_k - \Delta \tau_s. \tag{37}$$

C. Frequency-Domain Validation Results

The frequency-domain experiment shows that the DOB improves mechanical impedance rendering performance. Bode plots comparing the DOB On/Off cases vs the nominal behavior are shown in Fig. 3, and key metrics are captured in Tab. III. The DOB performed especially well at low frequency, $f=0.5~{\rm Hz}$, yielding a combined RMSPE of 8.9%, compared to a combined RMSPE of 36.3% with no DOB. Although performance decreased at higher frequencies, the DOB controller still outperformed the no DOB case across all frequency ranges.

D. Time-Domain Demonstration Results

The time domain experiment (Fig. 4) clearly demonstrates the two-fold capability of the controller: 1) it successfully tracks knee angle and torque trajectories during nominal conditions and 2) it accurately renders the desired biological impedance when the joint experiences a perturbation. Using (37), the impedance accuracy RMSE was 4.17 Nm for the time-domain perturbation test.

¹As reported in [45], the walking speed corresponding to our time domain signals (when denormalized with a 1.2-second duration) is slightly slower than comfortable barefoot walking.

IV. DISCUSSION

The DOB improved the rendering of mechanical impedance in the simulated prosthetic application, yielding significant reductions in both magnitude and phase errors, however, open issues still remain.

The controller admittedly struggled at higher frequencies as a direct consequence of a low DOB cutoff frequency $f_q = \omega/2\pi$. In theory, we should have been able to increase f_q up to the Nyquist frequency independent of the FSF gains or chosen trajectory while also preserving stability. But in practice, this did not hold. By trial and error, the DOB was found to be stable for $f_q \leq 10$ Hz and $\zeta = 0.7$ during the frequency domain wavelet tests, and $f_q \leq 5$ Hz and $\zeta = 1.5$ for the level walking time domain test. This may be due to the assumption that the disturbance is completely uncorrelated with the state vector, which is likely not held in practice. Judging from the DOB Off behavior in the frequency domain plot, the chief disturbance appears to have been some nonlinear frictional effect. This is because the low frequency spring asymptote is reduced in magnitude, yet maintains a nonzero phase lag—similar to hysteretic damping models or complex stiffness [44]. This tracks with observations made in manually back-driving the gear system, and extremely rapid decay of free-spinning motion. Our low-frequency DOB was certainly helpful in reducing the effect of this disturbance on rendered impedance below its cutoff frequency, but future versions of the system should be able to achieve better performance by investigating the bandwidth limit on the DOB more carefully and re-considering or working around the independence assumption on the disturbance.

Different FSF controller settings produce different levels of sensitivity to the transmission friction, and therefore different levels of importance for the DOB which compensates for this friction. Low impedance behaviors that result from greater utilization of the spring feedback terms K_2 and B_2 will naturally attenuate the friction disturbance due to this spring feedback alone. And negative spring feedback gains (used to produce stiffer-than-passive impedance) amplify the disturbance. Thus, by careful design of the actuator it may be possible to avoid the DOB component of the controller, and (equivalently) by introducing a DOB it may be possible to overcome the mechanical limits of a design.

When bench-marked against human perception, the DOB performs well. According to [46], the smallest change in knee stiffness an able-bodied human can reliably detect is $\sim 13\%$. Another study demonstrated below-knee amputees can perceive changes in ankle stiffness as low as 7.7% [47]. Although neither are an exact comparison, the DOB controller magnitude RMSPE of 7.2% at f=0.5 Hz (essentially a DC gain error metric corresponding to stiffness) was below both of these thresholds. A step in the right direction for biomimetic actuators, future iterations will seek to improve on this design further by driving impedance error below human perception across a wider frequency range.

These results are also significantly better than state-of-theart open loop impedance control performed in [19], which showed stiffness errors that reached up to 42% when the actuator included a large transmission ratio. While the authors discuss a solution capable of reducing stiffness errors to a mere 2.9%, it required characterizing disturbances offline and manually tuning feed-forward correction factors. This strategy also compensated for the nonlinear disturbance by changing the linear controller, without necessarily evaluating how this would impact performance at magnitudes other than the one tested in their system identification. In contrast, our DOB framework provides a way to accurately attenuate low frequency disturbances online, without the need for manually tuning feed-forward friction terms. While we also perform system identification at a single amplitude, the DOB attenuates non-LTI behavior (at low frequencies).

V. Conclusion

At frequencies below the DOB's cutoff, our control framework significantly improved the ability of the FSF controller to accurately render mechanical impedance despite the friction in the system. At very low frequencies (i.e. the region of the bode plot corresponding solely to stiffness) we achieved an RMSPE magnitude error of 7.2%. Performance at higher frequencies was less impressive, and unexpected instability prevented an increase in the bandwidth of the DOB. Despite this limitation, the system was also able to demonstrate the intended superposition of a biomechanical trajectory with a perturbation response.

REFERENCES

- K. Ziegler-Graham, E. J. MacKenzie, P. L. Ephraim, T. G. Travison, and R. Brookmeyer, "Estimating the prevalence of limb loss in the united states: 2005 to 2050," *Arch. Phys. Med. Rehab.*, vol. 89, no. 3, pp. 422– 429, 2008.
- [2] A. F. Azocar, L. M. Mooney, J.-F. Duval, A. M. Simon, L. J. Hargrove, and E. J. Rouse, "Design and clinical implementation of an open-source bionic leg," *Nat. Biomed. Eng.*, pp. 1–13, 2020.
- [3] W. Miller, A. Deathe, M. Speechley, and J. Koval, "The influence of falling, fear of falling, and balance confidence on prosthetic mobility and social activity among individuals with a lower extremity amputation," *Arch. Phys. Med. Rehab.*, vol. 82, no. 9, pp. 1238–1244, 2001.
- [4] B. J. Hafner and D. G. Smith, "Differences in function and safety between medicare functional classification level-2 and-3 transfemoral amputees and influence of prosthetic knee joint control." J. Rehab. Research & Dev., vol. 46, no. 3, 2009.
- [5] R. Gehlhar, M. Tucker, A. J. Young, and A. D. Ames, "A review of current state-of-the-art control methods for lower-limb powered prostheses," *Ann. Rev. Control*, vol. 55, pp. 142–164, 2023.
- [6] N. Hogan, "Impedance control: An approach to manipulation: Part I—theory," J. Dyn. Sys. Meas. Control, vol. 107, no. 1, pp. 8–16, 1985.
- [7] B. E. Lawson, J. Mitchell, D. Truex, A. Shultz, E. Ledoux, and M. Gold-farb, "A robotic leg prosthesis: Design, control, and implementation," *IEEE Robot. Auto. Magazine*, vol. 21, no. 4, pp. 70–81, 2014.
- [8] N. A. Kumar, W. Hong, and P. Hur, "Control of a transfemoral prosthesis on sloped terrain using continuous and nonlinear impedance parameters," in *IEEE Int. Conf. Robot. Auto.*, 2021, pp. 3219–3225.
- [9] T. K. Best, C. G. Welker, E. J. Rouse, and R. D. Gregg, "Data-driven variable impedance control of a powered knee–ankle prosthesis for adaptive speed and incline walking," *IEEE Trans. Robotics*, vol. 39, no. 3, pp. 2151–2169, 2023.
- [10] C. G. Welker, T. K. Best, and R. D. Gregg, "Improving sit/stand loading symmetry and timing through unified variable impedance control of a powered knee-ankle prosthesis," *IEEE Trans. Neural Sys. Rehab. Eng.*, vol. 31, pp. 4146–4155, 2023.
- [11] R. J. Cortino, T. K. Best, and R. D. Gregg, "Data-driven phase-based control of a powered knee-ankle prosthesis for variable-incline stair ascent and descent," *IEEE Trans. Medical Robotics and Bionics*, vol. 6, no. 1, pp. 175–188, 2024.

- [12] W. Hong and H. H. Huang, "Towards personalized control for powered knee prostheses: Continuous impedance functions and pca-based tuning method," in *Int. Conf. Rehab. Robot.* IEEE, 2023, pp. 1–6.
- [13] N. Hogan, "Adaptive control of mechanical impedance by coactivation of antagonist muscles," *IEEE Trans. Auto. Control*, vol. 29, no. 8, pp. 681–690, 1984.
- [14] E. J. Rouse, L. J. Hargrove, E. J. Perreault, and T. A. Kuiken, "Estimation of human ankle impedance during the stance phase of walking," IEEE Trans. Neural Sys. Rehab. Eng., vol. 22, no. 4, pp. 870–878, 2014.
- [15] H. Lee and N. Hogan, "Time-varying ankle mechanical impedance during human locomotion," *IEEE Trans. Neural Sys. Rehab. Eng.*, vol. 23, no. 5, pp. 755–764, 2014.
- [16] A. L. Shorter and E. J. Rouse, "Mechanical impedance of the ankle during the terminal stance phase of walking," *IEEE Trans. Neural Sys. Rehab. Eng.*, vol. 26, no. 1, pp. 135–143, 2017.
- [17] E. J. Rouse, R. D. Gregg, L. J. Hargrove, and J. W. Sensinger, "The difference between stiffness and quasi-stiffness in the context of biomechanical modeling," *IEEE Trans. Biomed. Eng.*, vol. 60, no. 2, pp. 562–568, 2012.
- [18] T. Elery, S. Rezazadeh, C. Nesler, and R. D. Gregg, "Design and validation of a powered knee–ankle prosthesis with high-torque, lowimpedance actuators," *IEEE Trans. Robotics*, vol. 36, no. 6, pp. 1649– 1668, 2020.
- [19] A. F. Azocar and E. J. Rouse, "Characterization of open-loop impedance control and efficiency in wearable robots," *IEEE Robot. Auto. Letters*, vol. 7, no. 2, pp. 4313–4320, 2022.
- [20] G. A. Pratt and M. M. Williamson, "Series elastic actuators," in IEEE/RSJ Int. Conf. Intel. Robot. Sys., vol. 1. IEEE, 1995, pp. 399–406.
- [21] M. Grimmer and A. Seyfarth, "Stiffness adjustment of a series elastic actuator in an ankle-foot prosthesis for walking and running: The tradeoff between energy and peak power optimization," in *IEEE Int. Conf. Robot. Auto.*, 2011, pp. 1439–1444.
- [22] E. J. Rouse, L. M. Mooney, and H. M. Herr, "Clutchable serieselastic actuator: Implications for prosthetic knee design," *Int. J. Robot. Research*, vol. 33, no. 13, pp. 1611–1625, 2014.
- [23] E. A. Bolívar Nieto, S. Rezazadeh, and R. D. Gregg, "Minimizing energy consumption and peak power of series elastic actuators: A convex optimization framework for elastic element design," *IEEE/ASME Trans. Mechatronics*, vol. 24, no. 3, pp. 1334–1345, 2019.
- [24] H. Vallery, R. Ekkelenkamp, H. Van Der Kooij, and M. Buss, "Passive and accurate torque control of series elastic actuators," in *IEEE/RSJ Int. Conf. Intel. Robot. Sys.*, 2007, pp. 3534–3538.
- [25] A. Albu-Schäffer, C. Ott, and G. Hirzinger, "A unified passivity-based control framework for position, torque and impedance control of flexible joint robots," *Int. J. Robot. Research*, vol. 26, no. 1, pp. 23–39, 2007.
- [26] N. L. Tagliamonte, D. Accoto, and E. Guglielmelli, "Rendering viscoelasticity with series elastic actuators using cascade control," in *IEEE Int. Conf. Robot. Auto.*, May 2014, pp. 2424–2429.
- [27] C. Ott, A. Albu-Schäffer, A. Kugi, and G. Hirzinger, "On the passivity–based impedance control of flexible joint robots," *IEEE Trans. Robotics*, vol. 24, no. 2, pp. 416–429, 2008.
- [28] D. Kim, Y. Zhao, G. Thomas, B. R. Fernandez, and L. Sentis, "Stabilizing series-elastic point-foot bipeds using whole-body operational space control," *IEEE Trans. Robotics*, vol. 32, no. 6, pp. 1362–1379, 2016.
- [29] N. Paine, J. S. Mehling, J. Holley, N. A. Radford, G. Johnson, C.-L. Fok, and L. Sentis, "Actuator control for the nasa-jsc valkyrie humanoid robot: A decoupled dynamics approach for torque control of series elastic robots," *J. Field Robotics*, vol. 32, no. 3, pp. 378–396, 2015.
- [30] A. Albu-Schäffer and G. Hirzinger, "State feedback controller for flexible joint robots: A globally stable approach implemented on dlr's

- light-weight robots," in *IEEE/RSJ Int. Conf. Intel. Robot. Sys.*, vol. 2. IEEE, 2000, pp. 1087–1093.
- [31] —, "Cartesian impedance control techniques for torque controlled light-weight robots," in *IEEE Int. Conf. Robot. Auto.*, vol. 1, 2002, pp. 657–663.
- [32] C. Ott, A. Albu-Schäffer, A. Kugi, S. Stamigioli, and G. Hirzinger, "A passivity based cartesian impedance controller for flexible joint robots-part I: Torque feedback and gravity compensation," in *IEEE Int. Conf. Robot. Auto.*, vol. 3, 2004, pp. 2659–2665.
- [33] K. Kong, J. Bae, and M. Tomizuka, "Control of rotary series elastic actuator for ideal force-mode actuation in human-robot interaction applications," *IEEE/ASME Trans. Mechatronics*, vol. 14, no. 1, pp. 105– 118, Feb 2009.
- [34] N. Paine, S. Oh, and L. Sentis, "Design and control considerations for high-performance series elastic actuators," *IEEE/ASME Trans. Mecha*tronics, vol. 19, no. 3, pp. 1080–1091, 2014.
- [35] J. S. Mehling, J. Holley, and M. K. O'Malley, "Leveraging disturbance observer based torque control for improved impedance rendering with series elastic actuators," in *IEEE/RSJ Int. Conf. Intel. Robot. Sys.*, 2015, pp. 1646–1651.
- [36] W. F. Rampeltshammer, A. Keemink, and H. Van Der Kooij, "An improved force controller with low and passive apparent impedance for series elastic actuators," *IEEE/ASME Trans. Mechatronics*, 2020.
- [37] L. Le-Tien, A. Albu-Schäffer, A. De Luca, and G. Hirzinger, "Friction observer and compensation for control of robots with joint torque measurement," in *IEEE/RSJ Int. Conf. Intel. Robot. Sys.* IEEE, 2008, pp. 3789–3795.
- [38] G. C. Thomas, J. M. Coholich, and L. Sentis, "Compliance shaping for control of strength amplification exoskeletons with elastic cuffs," in *IEEE/ASME Int. Conf. Adv. Intel. Mechatronics*. IEEE, 2019, pp. 1199–1206.
- [39] G. C. Thomas, J. S. Mehling, J. Holley, and L. Sentis, "Phase-relaxed-passive full state feedback gain limits for series elastic actuators," *IEEE/ASME Trans. Mechatronics*, vol. 26, no. 1, pp. 586–591, 2020.
- [40] U. H. Lee, C.-W. Pan, and E. J. Rouse, "Empirical characterization of a high-performance exterior-rotor type brushless dc motor and drive," in *IEEE/RSJ Int. Conf. Intel. Robot. Sys.* IEEE, 2019, pp. 8018–8025.
- [41] U. H. Lee, T. Shepherd, S. Kim, A. De, H. Su, R. Gregg, L. Mooney, and E. Rouse, "How to model brushless electric motors for the design of lightweight robotic systems," arXiv, 2023. [Online]. Available: https://doi.org/10.48550/arXiv.2310.00080
- [42] S. Li, J. Yang, W.-H. Chen, and X. Chen, *Disturbance observer-based control: methods and applications*. CRC press, 2014.
- [43] S. Pfeifer, R. Riener, and H. Vallery, "Knee stiffness estimation in physiological gait," in 2014 36th Ann. Int. Conf. of the IEEE Eng. in Medicine and Biology Society, 2014, pp. 1607–1610.
- [44] B. He, H. Huang, G. C. Thomas, and L. Sentis, "A complex stiffness human impedance model with customizable exoskeleton control," *IEEE Trans. Neural Sys. Rehab. Eng.*, vol. 28, no. 11, pp. 2468–2477, 2020.
- [45] R. Riener, M. Rabuffetti, and C. Frigo, "Stair ascent and descent at different inclinations," *Gait & Posture*, vol. 15, no. 1, pp. 32–44, 2002.
- [46] A. F. Azocar and E. J. Rouse, "Stiffness perception during active ankle and knee movement," *IEEE Trans. Biomed. Eng.*, vol. 64, no. 12, pp. 2949–2956, 2017.
- [47] M. K. Shepherd, A. F. Azocar, M. J. Major, and E. J. Rouse, "Amputee perception of prosthetic ankle stiffness during locomotion," *J. Neuroeng. Rehab.*, vol. 15, no. 1, pp. 1–10, 2018.